JOURNAL OF GEOPHYSICAL RESEARCH, VOL. 108, NO. A3, 1122, doi:10.1029/2002JA009624, 2003

Correction published 27 June 2003

Self-consistent magnetosphere-ionosphere coupling: Theoretical studies

G. V. Khazanov,[1] M. W. Liemohn,[2] T. S. Newman,[3] M.-C. Fok,[4] and R. W. Spiro[5]

Received 31 July 2002; revised 11 November 2002; accepted 2 January 2003; published 18 March 2003.

[1] A theoretical examination of the electrodynamical interaction between the ionosphere and the inner magnetosphere is presented. A self-consistent ring current (RC) model has been developed that couples the electron and ion magnetospheric dynamics with the calculation of the electric field. Two new features were taken into account in order to close the self-consistent magnetosphere-ionosphere coupling loop. First, in addition to the RC ions, we have solved an electron kinetic equation in our model. Second, using the relation of *Galand and Richmond* [2001], we have calculated the height integrated ionospheric conductances as a function of the precipitated high energy magnetospheric electrons and ions that are produced by our model. To validate the results of our model we simulate the magnetic storm of May 2, 1986, a storm that has been comprehensively studied by *Fok et al.* [2001], and have compared our results with different theoretical approaches. The self-consistent inclusion of the hot electrons and their effect on the conductance results in deeper penetration of the magnetospheric electric field. In addition, a slight westward rotation of the potential pattern (compared to previous self-consistent results) is evident in the inner magnetosphere. These effects change the hot plasma distribution, especially by allowing increased access of plasma sheet ions and electrons to low L shells. These results are consistent with recent observations from the IMAGE satellite. *INDEX TERMS:* 2736 Magnetospheric Physics: Magnetosphere/ionosphere interactions; 7807 Space Plasma Physics: Charged particle motion and acceleration; 2753 Magnetospheric Physics: Numerical modeling; 2730 Magnetospheric Physics: Magnetosphere—inner; *KEYWORDS:* magnetic storms, ring current, electric fields, numerical simulations

Citation: Khazanov, G. V., M. W. Liemohn, T. S. Newman, M.-C. Fok, and R. W. Spiro, Self-consistent magnetosphere-ionosphere coupling: Theoretical studies, *J. Geophys. Res.*, *108*(A3), 1122, doi:10.1029/2002JA009624, 2003.

1. Introduction

[2] Magnetosphere-ionosphere (MI) coupling has interested scientists for decades and, in spite of experimental and theoretical research efforts, is still one of the least well known dynamic processes in space plasma physics. The reason for this is that the numerous physical processes associated with MI coupling occur over multiple spatial lengths and temporal scales. One typical example of MI coupling is large-scale ring current electrodynamic coupling that includes calculation of the magnetospheric electric field that is consistent with the ring current (RC) distribution. A general scheme for numerical simulation of such large-scale magnetosphere-ionosphere coupling processes has been presented earlier in many works [see *Harel et al.*, 1981; *Wolf and Spiro*, 1984]. In the model used in those studies, the so-called Rice convection model (RCM), a Maxwellian form of the energy distribution of the particles and an isotropic pitch angle distribution in the plasma sheet are assumed. The mathematical formulation of this model is based on "modified frozen-in flux theorem" for an ensemble of adiabatically drifting particles in the magnetosphere. By tracking the flow of particles through the inner magnetosphere, the bounce-averaged phase space density of the hot ions and electrons can be reconstructed and the magnetospheric electric field can be calculated such that it is consistent with the particle distribution in the magnetosphere.

[3] Since the development of the RCM, there have been numerous other theoretical models of the flow of particles through the inner magnetosphere [e.g., *Takahashi et al.*, 1990; *Fok et al.*, 1993; *Chen et al.*, 1993; *Jordanova et al.*, 1996; *Khazanov et al.*, 1998; *Ebihara and Ejiri*, 1998]. While these models provide a better description of the velocity space distribution of the hot ions and electrons, none of them self-consistently calculates the electrodynamic coupling between the ionosphere and the magnetosphere. They instead apply either an analytical electric field descrip-

[1]National Space Science and Technology Center, NASA Marshall Space Flight Center, Huntsville, Alabama, USA.
[2]Space Physics Research Laboratory, University of Michigan, Ann Arbor, Michigan, USA.
[3]Computer Science Department, University of Alabama in Huntsville, Huntsville, Alabama, USA.
[4]Laboratory for Extraterrestrial Physics, NASA Goddard Space Flight Center, Greenbelt, Maryland, USA.
[5]Physics and Astronomy Department, Rice University, Houston, Texas, USA.

0148-0227/03/2002JA009624

tion (like the Volland-Stern model [*Volland*, 1973; *Stern*, 1975]) or an empirically derived convection pattern (such as that from the assimilative mapping of ionospheric electrodynamics (AMIE) technique [*Richmond and Kamide*, 1988] or the Weimer model [*Weimer*, 1995]). Recently, though, *Fok et al.* [2001] combined the RCM with their RC kinetic model in order to come up with a self-consistent description of the RC ion distribution and magnetospheric electric field. The model developed by *Liemohn et al.* [2002] describes large-scale electrodynamic coupling processes and provides a self-consistent simulation of RC ions, the magnetospheric electric field, and thermal plasma density. Both of these models use a Birkeland current distribution resulting from the closure of the partial RC, taking into account an arbitrary pitch angle distribution of hot ions, and use a semiempirical approach for the conductance calculation. However, the *Liemohn et al.* [2002] model is based on the magnetospheric electric field calculation developed by *Ridley and Liemohn* [2002], while the *Fok et al.* [2001] model is based on the coupling calculation of the RCM.

[4] The new model described below is a continuation of the work devoted to large-scale ionosphere-magnetosphere coupling. Two new features are taken into account in order to close a self-consistent magnetosphere-ionosphere coupling loop. First, we solve an electron kinetic equation in our model in addition to those for the RC ions, coupling all of these species through a self-consistent electric field calculation. Second, we calculate the height-integrated ionospheric conductances as a function of the precipitated high-energy magnetospheric electrons and ions that are produced by our model, using the precipitation-conductance formulation of *Galand and Richmond* [2001]. To validate the results of our model we simulate the magnetic storm of 2 May 1986. This storm has been comprehensively studied by *Fok et al.* [1996, 2001], and therefore it is useful to compare our results with the different theoretical approaches used in these studies.

[5] In the discussion below, the main focus is on the theoretical implications of these calculational modifications. The intent is to describe the influence of a self-consistent inclusion of the real distribution of hot electrons in the inner magnetosphere as well as the influence of a self-consistent ionospheric conductance pattern. As will be shown, these code changes result in interesting and significant alterations in the particle fluxes and the electric potential pattern. The plots are produced in a format similar to what has been shown previously [*Fok et al.*, 1996, 2001], and so comparisons against published data for this event are straightforward and left to the reader. In addition, there are still more improvements being made to the model to make the solution more realistic and robust. Thus this paper can be considered as a progress report on the status of the model, showing preliminary results of the dramatic changes resulting from the modifications made to date.

2. Model Description

[6] A self-consistent solution for the interaction of the ionosphere and the inner magnetosphere is achieved by solving equations for the particle distribution in the magnetosphere simultaneously with an equation for the mid-latitude ionospheric potential. A schematic diagram of the computational algorithm is shown in Figure 1. From the magnetospheric particle solvers driven by the electric and magnetic fields, precipitation fluxes are used to find the ionospheric conductance and Birkeland currents are used as inputs to the ionospheric current system calculation. From the potential solver, electric fields are derived that are used in the next time step of the magnetospheric solver. Let us discuss each component of this diagram in more detail.

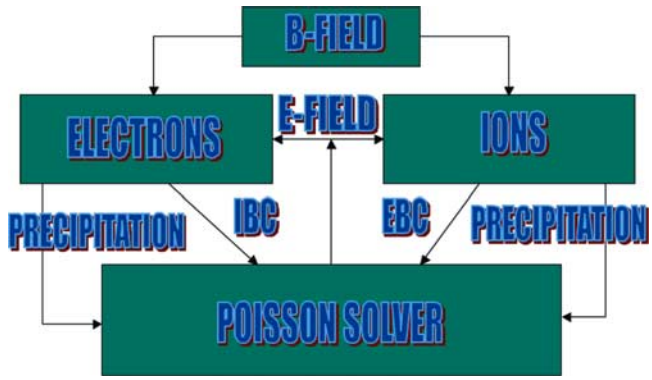

Figure 1. Schematic flow diagram of the computational approach. Driven by the electric and magnetic fields, equation (1) is solved for the electrons and ions. From these results, particle precipitation fluxes are calculated to determine the ionospheric conductances as well as Birkaland currents (IBC and EBC) as inputs to the Poisson solver. Equation (2) is used to find the ionospheric potential distribution, and by mapping these along the field lines, new magnetospheric electric fields are derived for use in the kinetic equation coefficients.

[7] We simulate the hot magnetospheric plasma dynamics by solving the bounce-averaged kinetic equation for the phase space distribution function, Q, of the RC ion species (H^+ and O^+), and electrons

$$\frac{\partial Q_\alpha}{\partial t} + \frac{1}{R_o^2}\frac{\partial}{\partial R_o}\left(R_o^2\left\langle\frac{dR_o}{dt}\right\rangle Q_\alpha\right) + \frac{\partial}{\partial \varphi}\left(\left\langle\frac{d\varphi}{dt}\right\rangle Q_\alpha\right) + \frac{1}{\sqrt{E}}\frac{\partial}{\partial E}\left(\sqrt{E}\left\langle\frac{dE}{dt}\right\rangle Q_\alpha\right) + \frac{1}{f(\mu_o)\mu_o}\frac{\partial}{\partial \mu_o} \cdot \left(f(\mu_o)\mu_o\left\langle\frac{d\mu_o}{dt}\right\rangle Q_\alpha\right) = \left\langle\frac{\delta Q_\alpha}{\delta t}\right\rangle_{\text{collis}} \qquad \alpha = e, H^+, O^+ \quad (1)$$

as a function of position in the magnetic equatorial plane (R_0, φ); kinetic energy and the cosine of the equatorial pitch angle (E, μ_0); and time t. In the left-hand side of this equation, all of the bounce-averaged drift velocities are shown in angle brackets and include all electric and magnetic drifts. These velocities, one for each independent variable in the calculation, will be determined from a number of electric field descriptions, to be discussed below. The $f(\mu_0)$ variable is a bounce-averaging coefficient defined by *Ejiri* [1978] that ranges from 0.8 to 1.3. The term on the right-hand side of equation (1) includes losses from charge exchange (only for H^+ and O^+ ions), Coulomb collisions, and precipitation at low altitudes (assumed lost at 800 km altitude along each field line). Each of the drift and loss terms is dependent on spatial location, energy, and pitch

angle and can be different for each species. Charge exchange and atmospheric loss are both treated as attentuation factors on the distribution function, while Coulomb collisions are described through an energy advection term (loss only) and a pitch angle diffusion term. The formulations for these processes are the same as those discussed by *Jordanova et al.* [1996] (see their equations (5)–(9)). Pitch angle diffusion into the loss cone resulting from interactions with the whistler mode waves in the plasmasphere is believed to be responsible for removing electrons from the slot region [*Lyons et al.*, 1972]. We took appropriate (for our energy range) loss timescales for this process from that study. Diffusion of ions by plasma waves was neglected in the present study. The source of the RC particles is inflow through the nightside outer simulation domain boundary. Loss through the dayside magnetopause is also taken into account, allowing free outflow of the RC electrons and ions from the simulation domain. More details regarding equation (1) are given by *Jordanova et al.* [1996, 1997], *Khazanov et al.* [1998, 1999], *Liemohn et al.* [2001a], and references therein.

[8] Together with the system of equations (1), we solve the Poisson's equation to determine the cross-field potential Φ throughout the ionosphere region [*Vasyliunas*, 1970]:

$$\nabla\left(-\overleftrightarrow{\Sigma}\nabla\Phi\right) = \sum_{\alpha} J_{\|\alpha}\sin I, \qquad (2)$$

where $\overleftrightarrow{\Sigma}$ is the tensor representing ionospheric Hall and Pederson height-integrated conductance in both hemispheres that is an analytical function of atmospheric precipitated electron and ion fluxes (the recent work by *Galand and Richmond* [2001] contains details) that we calculate in this model, $J_{\|\alpha}$ is the Birkeland current of the α component into the ionosphere that is calculated based on the phase space distribution function that was found from equation (1), and I is the inclination of the magnetic field. The relationship of *Galand and Richmond* [2001] for $\overleftrightarrow{\Sigma}$ assumed Maxwellian distributions for the precipitating fluxes. In our case, the particles have loss cone energy and pitch angle distributions according to the solution of equation (1), and so we fitted our numerical results with several Maxwellians in order to use their formulation. We only included Maxwellians with characteristic energies in the validity range stated by *Galand and Richmond* [2001], namely, 2–40 keV for the ions and 0.5–20 keV for the electrons. In addition, the conductance relationships of *Galand and Richmond* [2001] are valid only for proton and electron precipitation, so the oxygen ion precipitation is neglected in $\overleftrightarrow{\Sigma}$. Besides, oxygen ions are less efficient for ionization than protons. By using several Maxwellians, the modeled distributions can be fitted with an error of less than 5%, which is well within the 10% error of the *Galand and Richmond* [2001] parameterization technique. The solar contribution to the conductance is the same as that used by *Robinson et al.* [1987]. The calculation of $J_{\|\alpha}$ is very similar to that described by *Liemohn et al.* [2001b]; the Liemohn et al. calculation takes into account the spatial asymmetries, energy spectra, and pitch angle distributions resulting from the calculation. All three particle species (H^+, O^+ and e^-) are included in the summation in equation (2).

[9] By assuming equipotential field lines, ionospheric potentials from the solution of equation (2) are mapped out along the field lines and used in the next time step iteration to calculate the system of kinetic equations (1). This feedback of the potentials on the hot particle drifts results in a self-consistent calculation of the plasma distribution and the electric fields in the inner magnetosphere. To close a self-consistent magnetosphere-ionosphere coupling loop the solution of equation (1) generates the electron and ion precipitated fluxes that are used to calculate height-integrated ionospheric conductance based on the *Galand and Richmond* [2001] formulas.

[10] The numerical implementation of each equation of system (1) is done exactly as we discussed in our previous work (details are given by *Jordanova et al.* [1997]; *Khazanov et al.* [1998], and *Liemohn et al.* [2001a]). Briefly, the solution of equation (1) is obtained by allowing the phase space density of each species in each grid cell to be advected, diffused, and attenutated according to second-order numerical schemes. The numerical solution of equation (2) is based on the mathematical algorithm of the RCM that we adapted here based on work by *Fok et al.* [2001]. To ensure a high performance of our new model, we utilize a parallel processing approach that was developed by *Newman and Khazanov* [2002]. The parallel approach allows near-real-time computation of results on a small multiprocessor computer. The approach can be classified as a coarsely granular solution. It has two stages at each time step T_i. In the first stage, equation (1) is solved independently for each particle species (H+, O+, and electrons). Specifically, equation (1) for a species α is computed on a CPU C_α. In the second stage, the total Birkeland current, as described by the right-hand side of equation (2), at the time step T_i is assembled on a single "master" CPU, which then solves equation (2) for the cross-field potential Φ throughout the ionospheric region. Assembly requires each species' phase space distribution to be communicated to the "master" CPU. Advancement to the next time step T_{i+1} occurs only after the solution has been communicated by the "master" to all participating CPUs. The overall computational scheme is graphically represented in Figure 1, showing the feedback between the solutions of equations (1) and (2).

[11] The parallel approach has been achieved via the use of the highly portable Message Passing Interface (MPI) on a 16-processor SGI Origin machine at the Marshall Space Flight Center. The MPI has been used to achieve high performance in a wide variety of scientific problem areas [e.g., *Zhang and Newman*, 2001]. Each 15-s time step is computed in approximately 20 s on this machine.

[12] In this paper we simulate the main phase of the magnetic storm of 2 May 1986 that has been comprehensively studied and discussed by *Fok et al.* [1996, 2001]. We adapted the same initial and boundary conditions for H^+ RC ions as was discussed by these authors and used the dipole geomagnetic field configuration. The simulation domain we set up to be the same as Fok et al., from 44.5 to 67.2° magnetic latitude (L from 2 to 6.5 in a dipole magnetic field), and assumed an identical potential configuration at the poleward boundary. The boundary conditions for the O^+ RC ions that we used in this study were calculated using the paper by *Young et al.* [1982], relating

geosynchronous ion densities to the geomagnetic and solar activity as

$$O^+/H^+ = 4.5 \times 10^{-2} \exp(0.17Kp + 0.01F_{10.7}).$$

The initial condition for O^+ inside the boundary was found by using the H^+ initial condition and running the code with low magnetospheric activity (Kp = 1) for 2 days of simulation time. The resulting distribution has a very weak O^+ symmetric ring current (much smaller than the initial H^+ content of the preexisting symmetric ring current) with an additional small component of lower-energy O^+ ions out near the simulation domain outer boundary (also much smaller than the initial H^+ content). The initial O^+ distribution has essentially no impact on the simulation results.

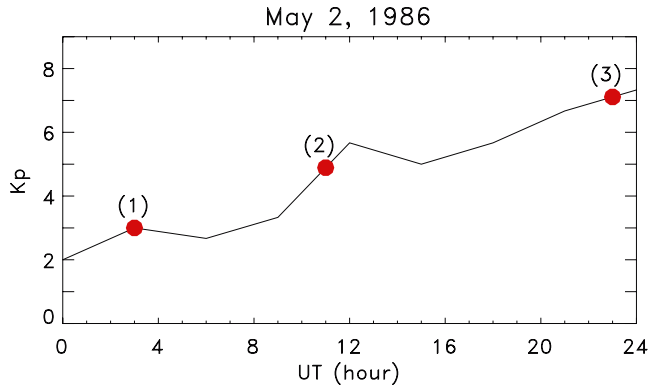

Figure 2. *Kp* history for 2 May 1986. Three times are indicated where the model results are shown and discussed.

3. Results

[13] The objective of this theoretical study is to examine the effects of the inclusion of hot electrons and self-consistent conductances on the development of the RC during a storm main phase. To quantitatively analyze this influence, the results from our code will be compared against a couple of benchmark calculations. In particular, we will show the similarities and differences of our results with those of the *Fok et al.* [2001] formulation, which also includes a self-consistent electric potential calculation, and the empirically derived Volland-Stern electric potential model.

[14] First, we should point out some of the numerical differences between our code and that of *Fok et al.* [2001]. Our code performs the particle calculation (solution of equation (1)) on a magnetospheric grid and the potential calculation (solution of equation (2)) on a grid defined by the ionospheric foot points of the magnetospheric spatial grid. The *Fok et al.* [2001] model performs both calculations on a spatial grid in the ionosphere. In addition, the two models solve over different velocity space variables and have different numerical approaches. Another difference is that the Fok et al. formulation used the RCM conductance model that superimposes a *Hardy et al.* [1987] auroral enhancement on a background conductance. Because one of the goals of our study is to come up with a self-consistent description of MI coupling, we used another approach and calculated height-integrated ionospheric conductances based on the electron and ion precipitation predicted by our model by applying the formulas of *Galand and Richmond* [2001]. We achieved good agreement with the results presented by *Fok et al.* [2001] when we ran our model only for RC H^+ ions and used the RCM conductance model. These results will be used in this section as a benchmark for our studies and will be called the *Fok et al.* [2001] results (even though they are results from our model, the code was set up to match their calculational mode). The other benchmark for the presented model will be a comparison of our results with the corresponding fluxes using a Volland-Stern magnetospheric electric field [*Volland*, 1973; *Stern*, 1975]. On the basis of a recommendation of *Fok et al.* [1996] we used this model with the shielding factor $\gamma = 2$, and with the offset equal to 2 hours in MLT eastward in order to get a best fit the charge-energy-mass (CHEM) instrument measurements (details are given by *Fok et al.* [2001]). In the figures below, results from all three of these approaches are shown. Again, these are results from our code, but set up with the *Kp*-prescribed Volland-Stern electric field description.

[15] The *Kp* history of the magnetic storm of 2 May 1986 is shown in Figure 2. This storm had an exceptionally long main phase, with a rising *Kp* value throughout 2 May. The three labeled times in Figure 2 are those selected to illustrate the results of our simulations, representing low, medium, and high levels of convection electric field strength. Note that the curve drawn in Figure 2 is the *Kp* history (continuously varying in time) used in the simulations presented below. This choice was made so our results would be comparable to those of *Fok et al.* [2001].

[16] All three of the simulation approaches have the same high-latitude boundary condition for the electric potential difference. This value is time-varying, changing with the *Kp* history during the event, as calculated by the Volland-Stern model. In the Volland-Stern simulations the convection potential inside the simulation domain is prescribed by their empirical formulation. For the other two techniques this potential difference is used as a high-latitude boundary condition and then equation (2) is solved self-consistently in the ionospheric simulation domain (however, with different field-aligned currents and conductances).

[17] Figure 3 shows the electric potential isocontours from the model for the three selected times on 2 May 1986 (the three columns). The three rows are the results for the three models: our formulation, the *Fok et al.* [2001] results, and a skewed Volland-Stern description. A critical feature in each of these potential contours is the Alfvén boundary, which is the last closed equipotential encircling the Earth. The shape of this contour provides a general description of the morphology of the potential distribution. In the Volland-Stern potential, all three patterns show the standard teardrop Alfvén boundary with everything rotated 2 hours eastward (with a stagnation point at 2000 LT in every plot). As *Kp* increases, the Alfvén boundary shrinks, but the morphology of the potential distribution is exactly the same in all three plots.

[18] In the *Fok et al.* [2001] potentials, there is noticeable twist to the potential pattern between the inner and outer

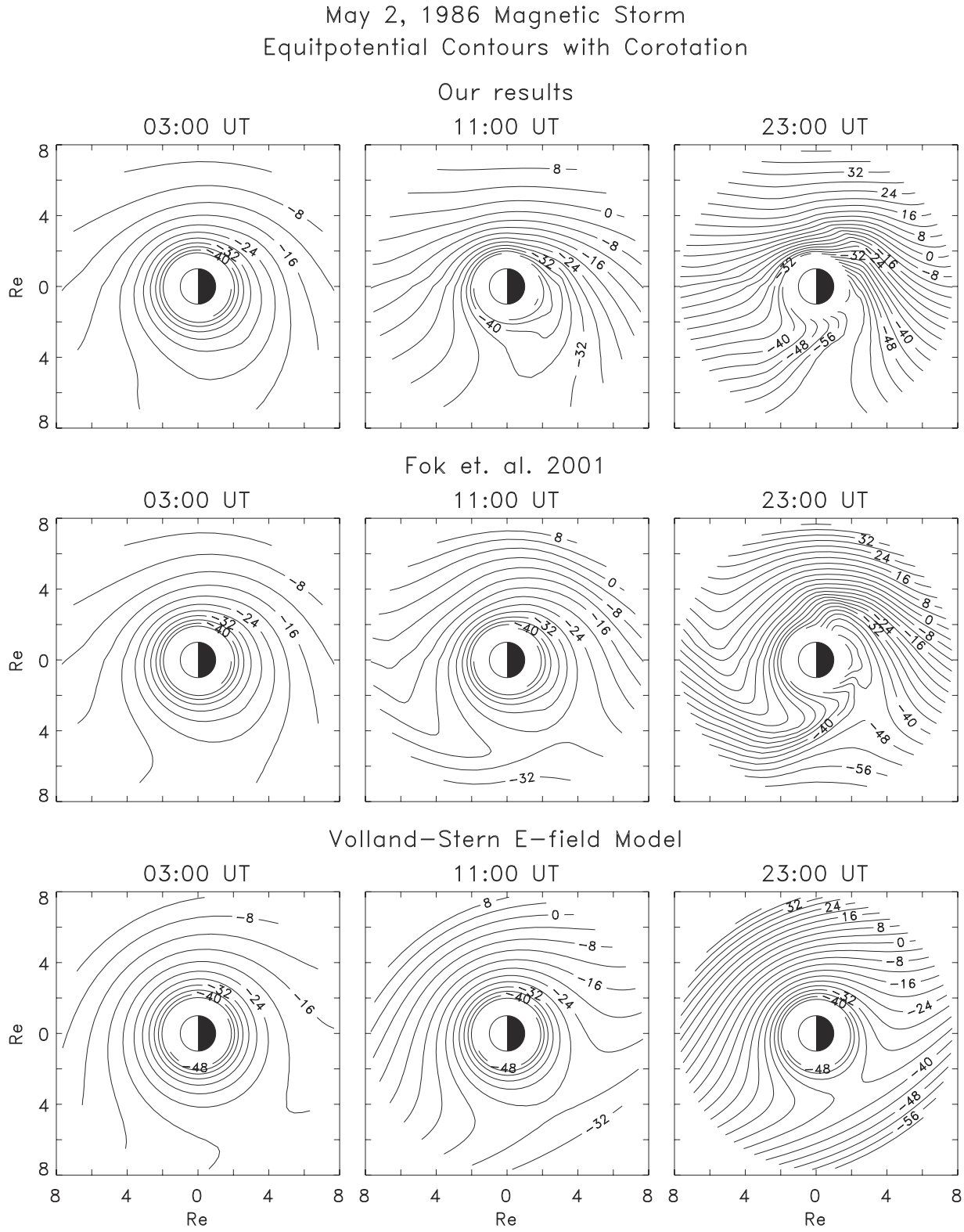

Figure 3. Equipotential contours at the three times highlighted in Figure 1 (the three columns) for our code's results (top row), the *Fok et al.* [2001] formulation (middle row), and a rotated Volland-Stern description (bottom row). The contour spacing is 4 kV, with the lines stopping at the magnetospheric simulation boundaries. In each plot, the Sun is to the left, dawn is to the top, dusk is to the bottom, and midnight is to the right.

portions of the simulation domain. That is, inside of $L = 4$, the potential pattern shows the ~2 hours rotation like that in the Volland-Stern potentials. Outside of this L shell, the pattern reverts to a straight dawn-to-dusk electric field configuration. As convection increases to high levels late on 2 May (right-hand column), the differential skew becomes bigger and this transition L shell moves inward. At this time, the Alfvén boundary is teardropped with the bulge pointed toward midnight (instead of pointed toward 2000 LT, as in the Volland-Stern model) but the outermost L shells are still oriented in a dawn-to-dusk configuration. The L shell of the transition between the midnight-centered teardrop morphology and the dawn-to-dusk field morphology is now actually inside of the last closed equipotential. Therefore the end of the teardrop is extended westward away from midnight, and the stagnation point is around 2200 LT. On the dayside, the Alfvén boundary is much closer to the Earth than it was in the Volland-Stern potential.

[19] Our results are more distorted than the *Fok et al.* [2001] potentials. This twisting of the closed equipotential is clearly seen for moderate *Kp* (middle column). At high *Kp*, the Alfvén boundary is close to $L = 2$, with only a small extension of the Alfvén boundary beyond this L shell in the premidnight region. This configuration for the Alfvén boundary is consistent with those seen in the IMAGE satellite data of the stormtime plasmasphere [*Sandel et al.*, 2001] and ring current [*Mitchell et al.*, 2001; *Pollock et al.*, 2001], particularly with respect to the nightside locations of plasma boundaries (e.g., the plasmapause and injection front). Equipotentials from near dusk at the outer boundary (as far around as 1900 LT) actually go around the dawnside of Earth, indicating a much greater local time extent of the plasma sheet that has access to the inner magnetosphere. In addition, the equipotential contours from our model are more closely spaced over a greater spatial region than those from the other models, indicating stronger electric fields deep in the inner magnetosphere.

[20] To understand the differences between these potential patterns, let us suppose we have hot ions and cold electrons (a traditional approach, such as that used by *Fok et al.* [2001]). While moving toward the Earth, the ions gradient-curvature drift westward, which produces a forbidden region. Cold electrons, while $\mathbf{E} \times \mathbf{B}$ drifting, will cross the boundary of this region. This spatial separation forms field-aligned currents and therefore increased conductance in the low-latitude ionosphere connected to this zone. The magnitude of field-aligned currents is approximately proportional to the total flux of cold electrons across the boundary. Now let us suppose that both the ions and electrons are hot (our approach). Because of the eastward gradient-curvature drift of the hot electrons, they do not penetrate as deeply into the inner magnetosphere as cold electrons. As a result, the flux of electrons across the boundary of the ion forbidden region is reduced, leading to a reduction of low-latitude precipitation and thus a reduction in conductance in this region. This results in better penetration of the electric field into the inner magnetosphere, as seen in our results.

[21] This is graphically illustrated in Figure 4. The solid curve is the Alfvén boundary for cold electrons in a $Kp = 6$ rotated Volland- Stern electric field. The dotted curve is the Alfvén boundary for typical hot ions in the same electric field (typical meaning ions with 7 keV of energy at $L = 6.6$ [e.g., *Birn et al.*, 1997; *Borovsky et al.*, 1998], increasing adiabatically inside of this location to 32 keV at $L = 4$ and up to 75 keV at $L = 3$). As plasma moves in from the nightside, the cold electrons will sweep eastward around the dawnside of the Earth, while the hot ions will drift westward around the duskside. The Alfvén boundaries are therefore the spatial cutoffs between the forbidden regions and the accessible regions for each of these species. The region inside of the dotted curve but outside of the solid curve is a place containing cold electrons but not hot ions. This is where the field-aligned currents will be located, with a strength proportional to the flux of electrons across the dotted line.

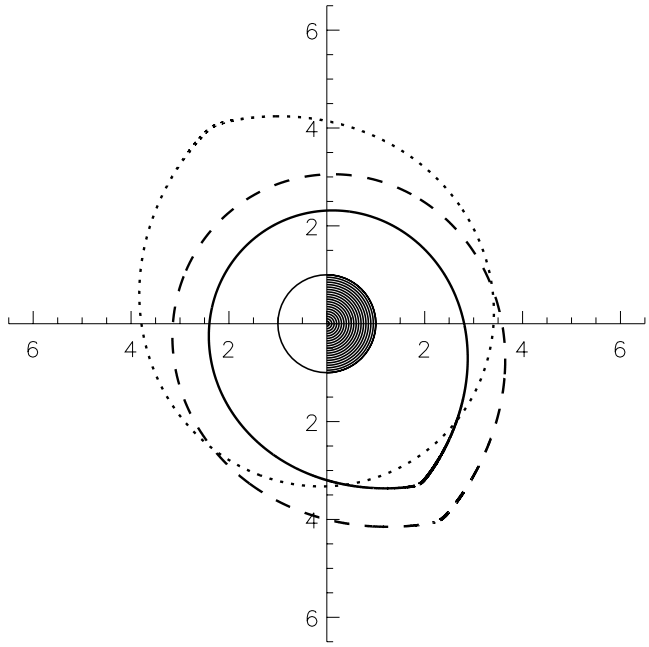

Figure 4. Alfvén boundaries for cold electrons (solid line), ions with 7 keV energy at $L = 6.6$ (dotted line), and electrons with 1 keV energy at $L = 6.6$ (dashed line). These curves denote the boundary between the forbidden region and the accessible region of the inner magnetosphere for particles approaching Earth from the nightside plasma sheet.

[22] In our new model we use the hot electron distribution in the inner magnetosphere for this field-aligned current intensity calculation. The dashed line is the Alfvén boundary for typical hot electrons in the same $Kp = 6$ rotated Volland-Stern field (typical meaning an energy of 1 keV at $L = 6.6$ [e.g. *Birn et al.*, 1997; *Borovsky et al.*, 1998], which adiabatically increases to 4.5 keV at $L = 4$ and 10.6 keV at $L = 3$). It is seen that the "electron-only" zone (inside of the dotted line but outside of the dashed line) is much smaller for this hot-electron assumption compared to the cold-electron case because of the extra eastward drift. Of course, Figure 4 is simply an example plot of these Alfvén boundaries. The real field-aligned current intensities are functions of the time history of the convection electric field and boundary particle fluxes. For the simulations with self-

consistent electric field calculations, these boundaries will not be simple teardrop shapes. The general concept, however, remains the same.

[23] Next we examine the influence of these differences in the potential distributions on the hot particle fluxes in the inner magnetosphere. Figure 5 shows the comparison of the instantaneous pitch angle-averaged H^+ fluxes at 0300 UT (blue lines), 1100 UT (green lines), and 2300 UT (red lines) of 2 May 1986 calculated by the three different approaches (different line styles and symbols). In order to compare our results with the *Fok et al.* [2001] simulations, we have used the same format for this figure as Figure 1 in their paper. The top row shows three locations in the late morning sector, while the bottom row shows three locations in the postmidnight sector. It should be noted, however, that Figure 1 of *Fok et al.* [2001] does not present instantaneous ion fluxes (as shown in our Figure 5). In order to compare their model with AMPTE/CCE measurements, *Fok et al.* [2001] presented their Figure 1 near the end (2000–2300 UT) of 2 May 1986 with averaging over the temporal and spatial scales. Therefore a direct comparison of the results presented here with those given by *Fok et al.* [2001] will reveal some differences, even though the *Fok et al.* [2001] model configuration is the same in both papers. Because the emphasis of this study is to investigate the impacts resulting from the inclusion of several modifications to the self-consistent magnetosphere-ionosphere coupling process, a direct comparison with AMPTE/CCE (or any other) observations will not be shown here. As the model is continued to be developed, such data-theory examinations will be conducted. However, as mentioned above, such penetration of the convection electric field is consistent with nightside plasma observations from the IMAGE satellite.

[24] The ion flux spectra reveal some interesting differences between the simulations. The biggest changes are seen in the green and red curves (moderate and high activity levels). The differences are substantial, particularly in the <100 keV energy range deep in the inner magnetosphere (middle and right-hand columns). Ions only have access to this volume of phase space through convection; the corotation and gradient-curvature drifts are in the azimuthal direction only. Therefore changes in the convection pattern intimately affect their distribution. The most obvious change is that the minimum of the spectra near 10 keV is shifted to lower energies in our results. At 2300 UT in Figure 5d, our results do not even show a low-energy cutoff because the convection is so strong that the entire energy range has access to this spatial location. At 2300 UT in Figure 5c, only our model shows a peak in the 10–100 keV energy range. In the other two formulations this spatial point is not convectively connected to the nightside source region for these energies. The high-energy end of the spectra (above 100 keV or so) is essentially unaffected by convection because their motion is dominated by the gradient-curvature drift. Likewise, the blue curves, which are the results for low convection (after only 1 hour of simulation time), show very little difference between the calculational approaches at all energies.

[25] Figure 6 shows the comparison of the pitch angle-averaged electron fluxes at 2100 UT of 2 May 1986 at the same time and space locations. Here we used the same line character to represent the results from the different simulations. The data presented here that correspond to the Fok et al. and Volland-Stern models are results from our model with *Fok et al.* [2001] and Volland-Stern convection, correspondingly. Note that the potential calculation of our model depends on both the hot ions and electrons for field-aligned currents and conductances, whereas the *Fok et al.* [2001] model only uses the hot ion fluxes for the field-aligned currents (with a specified conductance pattern), and the Volland-Stern model does not use any of the hot particle results for its potential distribution.

[26] The electron spectra in Figure 6 show far less difference between the convection formulations than did the ions in Figure 5. At the outer L shells (left-hand column), convective access is similar between the simulations and the spectra look alike. Moving to lower L shells, however, differences arise as convective access is limited to only the lower energy electrons. The differences are most clearly seen at 2300 UT (red curves), with our model's results allowing more electrons into the inner magnetosphere over a larger energy range. In Figures 6c and 6e, for instance, the electron flux in the 10–100 keV energy range is enhanced by up to 1.5 orders of magnitude. The peak near 20–40 keV is evidence of additional acceleration in the inner magnetosphere from the penetrating convection electric field. In Figure 6d, only our model produces an enhancement in the E < 10 keV electrons at this spatial location. This enhancement is due to of the altered electric field pattern allowing greater access to the inner magnetosphere.

[27] This model is the first calculation that self-consistently includes the dynamics of the real spatial, energy, and pitch angle distribution of the hot electrons in the calculation of the stormtime RC development and inner magnetospheric potential distribution. Even though our model produces larger hot electron fluxes in the inner magnetosphere than what is calculated by the other two approaches, the conductances are still smaller than in those models. This is because our conductances are based on the real electron precipitation rather than assuming something about this precipitation. This self-consistency modifies the potential distribution, which in turn modifies the hot plasma distribution in the inner magnetosphere. This dynamic feedback is seen here for the first time.

4. Summary

[28] In this study, a theoretical examination of the stormtime interaction between the ionosphere and the inner magnetosphere has been presented. The self-consistent ring current (RC) model that we have developed couples electron and ion magnetospheric dynamics with the calculation of the electric field. Two new features were taken into account in order to close the self-consistent magnetosphere-ionosphere coupling loop. First, in addition to the RC ions, we solve an electron kinetic equation in our model, self-consistently including these results in the solution. Second, using the relationships developed by *Galand and Richmond* [2001], we calculate the height-integrated ionospheric conductances as the function of precipitated high-energy magnetospheric electrons and ions as produced by our model. While others have performed

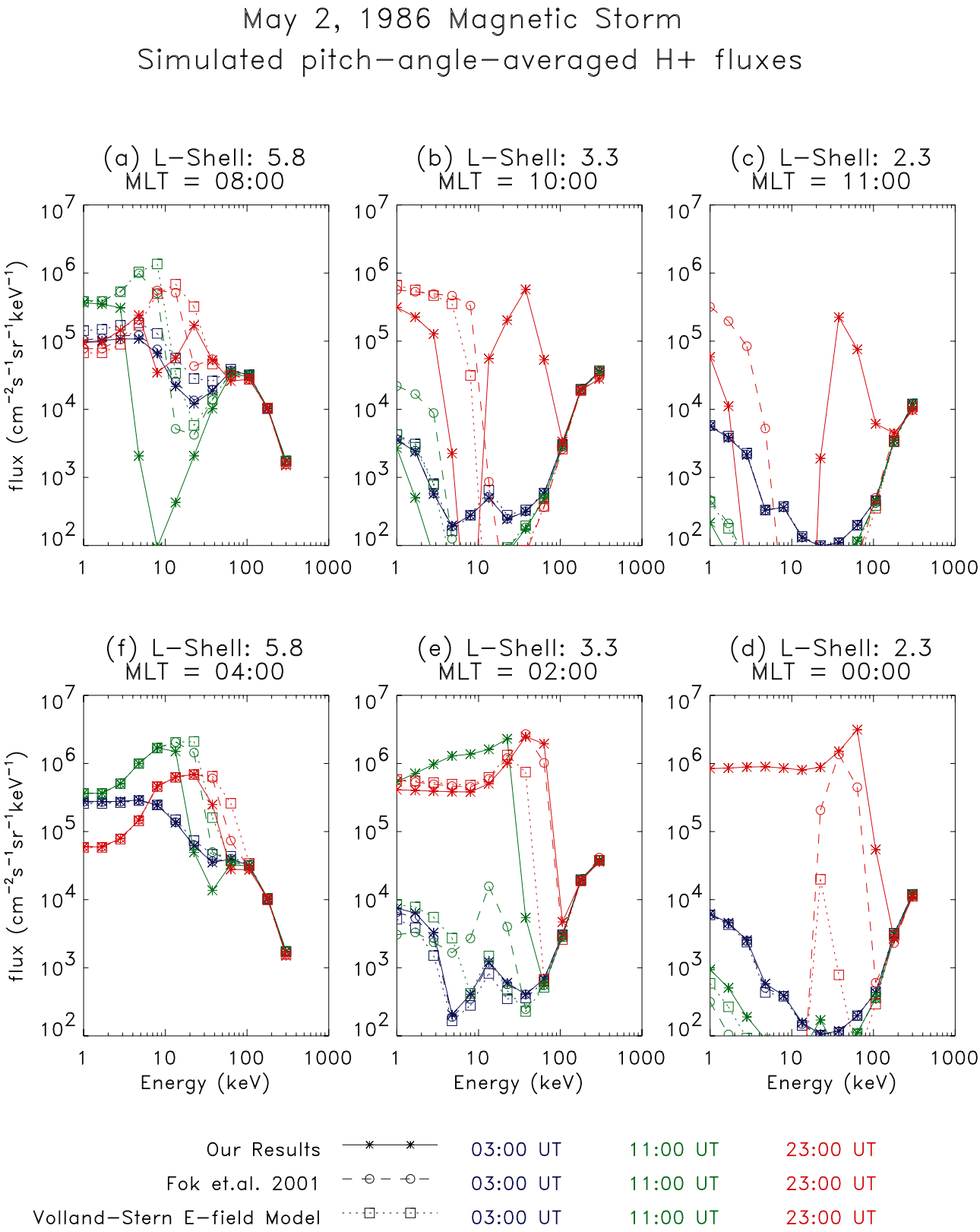

Figure 5. Pitch angle-averaged differential number flux of H^+ at six spatial locations in the inner magnetosphere. In the top row are points in the late-morning sector, and in the bottom row are points in the postmidnight sector. The legend at the bottom shows the different line styles and symbols used for the three convection formulations, and the three colors (blue, green, and red) indicate the universal time at which the spectra were taken from the simulation results (0300, 1100, and 2300 UT, respectively). Note that the bottom-row panels are labeled f through d, following *Fok et al.* [2001].

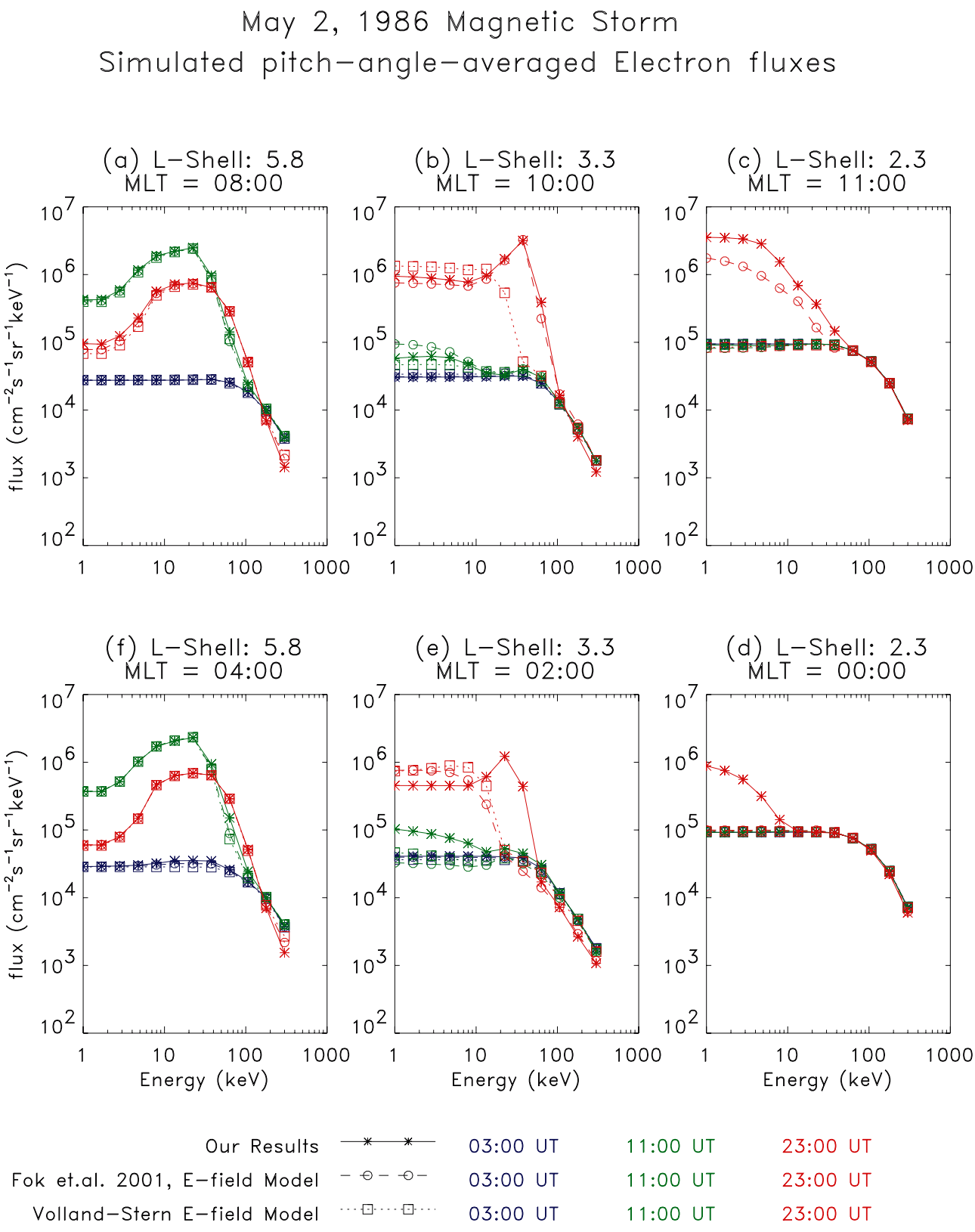

Figure 6. Same as Figure 5, except for electrons.

coupled calculations of the ionosphere and inner magnetosphere [e.g., *Wolf and Spiro*, 1984; *Fok et al.*, 2001; *Liemohn et al.*, 2002], these two components have not been included in the procedure. These additions result in fundamental changes to the electric potential pattern in the inner magnetosphere, with a smaller Alfvén boundary than previous potential formulations would predict but a boundary (especially on the nightside) consistent with recent

satellite observations [*Sandel et al.*, 2001; *Mitchell et al.*, 2001; *Pollock et al.*, 2001]. This leads to deeper penetration of the plama sheet ions and electrons into the inner mangetosphere and more effective ring current formation. The resulting field-aligned currents and precipitation fluxes dynamically change the potential pattern, resulting in additional alterations to the drifts.

[29] This study focused only on the theoretical aspects of the magnetosphere-ionosphere coupling process, showing changes in the simulation results from these code modifications. A more comprehensive analysis of the capabilities of this new model will be presented in a future study, including a thorough comparison against ionospheric and magnetospheric observations. One reason for waiting on this theory-data closure is that several more improvements are planned for the model, and a comparison against reality is premature. These additional modifications include a self-consistent coupling of the hot plasma distributions with plasma wave generation, propagation, and feedback. Our initial results of this wave-particle interaction analysis were presented by *Khazanov et al.* [2002]. It is planned to include not only ion cyclotron waves in this coupling process, but all relevant plasma wave frequencies and modes. Yet another modification is the self-consistent inclusion of the thermal plasma calculation, like the study of *Liemohn et al.* [2002]. Once these developments are completed, it is felt that the code will be ready for analyzing and interpreting geophysical observations. However, the present version of the model reveals an interesting effect on the convection pattern in the inner magnetosphere, resulting in more efficient inflow of the hot plasma sheet particles to this region.

[30] **Acknowledgments.** This work was supported by National Aeronautics and Space Administration (NASA) grants NAG5-4771, NAG5-6976, and NCC8-181.

[31] Arthur Richmond thanks Margaret W. Chen and Marina Galand for their assistance in evaluating this paper.

References

Birn, J., M. F. Thomsen, J. E. Borovsky, G. D. Reeves, D. J. McComas, and R. D. Belian, Characteristic plasma properties during dispersionless substorm injections at geosynchronous orbit, *J. Geophys. Res.*, *102*, 2309, 1997.

Borovsky, J. E., M. F. Thomsen, and R. C. Elphic, The driving of the plasma sheet by the solar wind, *J. Geophys. Res.*, *103*, 17,617, 1998.

Chen, M. W., M. Schulz, L. R. Lyons, and D. J. Gorney, Stormtime transport of ring current and radiation belt ions, *J. Geophys. Res.*, *98*, 3835, 1993.

Ebihara, Y., and M. Ejiri, Modeling of solar wind control of the ring current buildup: A case study of the magnetic storms in April 1997, *Geophys. Res. Lett.*, *25*, 3751, 1998.

Ejiri, M., Trajectory traces of charged particles in the magnetosphere, *J. Geophys. Res.*, *83*, 4798, 1978.

Fok, M.-C., J. U. Kozyra, A. F. Nagy, C. E. Rasmussen, and G. V. Khazanov, Decay of equatorial ring current ions and associated aeronomical consequences, *J. Geophys. Res.*, *98*, 19,381, 1993.

Fok, M.-C., T. E. Moore, and M. E. Greenspan, Ring current development during storm main phase, *J. Geophys. Res.*, *101*, 15,311, 1996.

Fok, M.-C., R. A. Wolf, R. W. Spiro, and T. E. Moore, Comprehensive computational model of Earth's ring current, *J. Geophys. Res.*, *106*, 8417, 2001.

Galand, M., and A. D. Richmond, Ionospheric electrical conductances produced by auroral proton precipitation, *J. Geophys. Res.*, *106*, 117, 2001.

Hardy, D. A., M. S. Gussenhoven, R. Raistrick, and W. J. McNeil, Statistical and functional representations of the pattern of auroral energy flux, number flux, and conductivity, *J. Geophys. Res.*, *92*, 12,275, 1987.

Harel, M., R. A. Wolf, P. H. Reiff, R. W. Spiro, W. J. Burke, F. J. Rich, and M. Smiddy, Quantitative simulation of a magnetospheric substorm, 1, Model logic and overview, *J. Geophys. Res.*, *86*, 2217, 1981.

Jordanova, V. K., L. M. Kistler, J. U. Kozyra, G. V. Khazanov, and A. F. Nagy, Collisional losses of ring current ions, *J. Geophys. Res.*, *101*, 111, 1996.

Jordanova, V. K., J. U. Kozyra, A. F. Nagy, and G. V. Khazanov, Kinetic model of the ring current-atmosphere interactions, *J. Geophys. Res.*, *102*, 14,279, 1997.

Khazanov, G. V., M. W. Liemohn, J. U. Kozyra, and T. E. Moore, Global superthermal electron transport: Photoelectron and plasma sheet electron sources, *J. Geophys. Res.*, *103*, 23,485, 1998.

Khazanov, G. V., M. W. Liemohn, E. N. Krivorutsky, J. M. Albert, J. U. Kozyra, and B. E. Gilchrist, Relativistic electron beam propagation in the Earth's magnetosphere, *J. Geophys. Res.*, *104*, 28,587, 1999.

Khazanov, G. V., K. V. Gamayunov, V. K. Jordanova, and E. N. Krivorutsky, A self-consistent model of the interacting ring current ions and electromagnetic ion cyclotron waves, initial results: Waves and precipitating fluxes, *J. Geophys. Res.*, *107*(A6), 1085, 10.1029/2001JA000180, 2002.

Liemohn, M. W., J. U. Kozyra, M. F. Thomsen, J. L. Roeder, G. Lu, J. E. Borovsky, and T. E. Cayton, Dominant role of the asymmetric ring current in producing the stormtime *Dst**, *J. Geophys. Res.*, *106*, 10,883, 2001a.

Liemohn, M. W., J. U. Kozyra, C. R. Clauer, and A. J. Ridley, Computational analysis of the near-Earth magnetospheric current system, *J. Geophys. Res.*, *106*, 29,531, 2001b.

Liemohn, M. W., D. L. Gallagher, D. M. Ober, A. J. Ridley, J. U. Kozyra, P. C:son Brandt, G. V. Khazanov, and M. L. Adrian, Nightside plasmasphere variations produced by the stormtime ring current, *Eos Trans. AGU*, *83*(19), Spring Meet. Suppl., Abstract SM42E-02, 2002.

Lyons, L. R., R. M. Thorne, and C. F. Kennel, Pitch-angle diffusion of radiation belt electrons with the plasmasphere, *J. Geophys. Res.*, *77*, 3455, 1972.

Mitchell, D. G., K. C. Hsieh, C. C. Curtis, D. C. Hamilton, H. D. Voss, E. C. Roelof, and P. C:son Brandt, Imaging two geomagnetic storms in energetic neutral atoms, *Geophys. Res. Lett.*, *28*, 1151, 2001.

Newman, T. S., and G. V. Khazanov, Self-consistent large-scale magnetosphere-ionosphere coupling: Computational aspects and experiments, in *2002 NASA/ASEE Faculty Fellowship Program*, edited by L. M. Freeman et al., pp. XXI-1–XXI-5, NASA, Washington, D. C., 2002.

Pollock, C. J., et al., Initial Medium Energy Neutral Atom (MENA) images of Earth's magnetosphere during substorms and storm-time, *Geophys. Res. Lett.*, *28*, 1147, 2001.

Richmond, A. D., and Y. Kamide, Mapping electrodynamic features of the high-latitude ionosphere from localized observations: Technique, *J. Geophys. Res.*, *93*, 5741, 1988.

Ridley, A. J., and M. W. Liemohn, A model-derived description of the penetration electric field, *J. Geophys. Res.*, *107*(A8), doi:10.1029/2001JA000051, 2002.

Robinson, R. M., R. R. Vondrak, K. Miller, T. Dabbs, and D. Hardy, On calculating ionospheric conductances from the flux and energy of precipitating electrons, *J. Geophys. Res.*, *92*, 2565, 1987.

Sandel, B. R., R. A. King, W. T. Forrester, D. L. Gallagher, A. L. Broadfoot, and C. C. Curtis, Initial Results from the IMAGE Extreme Ultraviolet Imager, *Geophys. Res. Lett.*, *28*, 1439, 2001.

Stern, D. P., The motion of a proton in the equatorial magnetosphere, *J. Geophys. Res.*, *80*, 595, 1975.

Takahashi, S., T. Iyemori, and M. Takeda, A simulation of the storm-time ring current, *Planet. Space Sci.*, *38*, 1133, 1990.

Vasyliunas, V. M., Mathematical models of magnetospheric convection and its coupling to the ionosphere, in *Particles and Fields in the Magnetosphere*, edited by B. M. McCormac, p. 60, D. Reidel. Norwell, Mass., 1970.

Volland, H., A semiempirical model of large-scale magnetospheric electric fields, *J. Geophys. Res.*, *78*, 171, 1973.

Weimer, D. R., Models of high-latitude electric potentials derived with a least error fit of spherical coefficients, *J. Geophys. Res.*, *100*, 19,595, 1995.

Wolf, R. A., and R. W. Spiro, Particle behaviour in the magnetosphere, in *Computer Simulation of Space Plasmas: Advances in Earth and Planetary Sciences*, p. 227, Terra Sci., Tokyo, 1984.

Young, D. T., H. Balsiger, and J. Geiss, Correlations of magnetospheric ion composition with geomagnetic and solar activity, *J. Geophys. Res.*, *87*, 9077, 1982.

Zhang, H., and T. S. Newman, High performance MIMD computation for out-of-core volume visualization, in *Proceedings, Supercomputing 2001 Conference (Poster Abstracts)*, Assoc. for Comput. Mach., New York, 2001.

M.-C. Fok, Laboratory for Extraterrestrial Physics, NASA Goddard Space Flight Center, Greenbelt, MD 20771, USA.

G. V. Khazanov, National Space Science and Technology Center, NASA Marshall Space Flight Center, Huntsville, A 35805, USA. (george.khazanov@msfc.nasa.gov)

M. W. Liemohn, Space Physics Research Laboratory, University of Michigan, Ann Arbor, MI 48176, USA.

T. S. Newman, Computer Science Department, University of Alabama in Huntsville, Huntsville, AL 35806, USA.

R. W. Spiro, Physics and Astronomy Department, Rice University, Houston, TX 77005, USA.